Attitude estimation for artillery shells using magnetometers and frequency detection of accelerometers

Aurélien Fiot, Sébastien Changey, Nicolas Petit

Version of Record: https://www.sciencedirect.com/science/article/pii/S0967066122000090
Manuscript_136fdf4dac887af853aa264e088c93c7

Attitude estimation for artillery shells using magnetometers and frequency detection of accelerometers

Aurélien Fiot[a,b], Sébastien Changey[a], Nicolas Petit[b,*]

[a] *French-German Research Institute of Saint-Louis, ISL, Guidance, Navigation and Control Dept., 5 rue du Général Cassagnou, Saint-Louis, 68300, France*
[b] *MINES ParisTech, PSL University, CAS - Centre Automatique et Systèmes, 60 bd St Michel, Paris, 75272, France*

Abstract

The article proposes a method to estimate the attitude of an artillery shell in free flight. It uses strapdown accelerometers and magnetometers, and circumvents the intrinsic inability of accelerometers to provide direction information during free flight by employing them not to measure the gravity but to estimate the velocity w.r.t. the air. This is achieved in an innovative way, through frequency detection applied to the pitch and yaw rotational dynamics generated by aerodynamic moments, directly visible on the accelerometers' signals. The determination of the shell's velocity without any ground-based position radar is a first contribution. The velocity variation gives information regarding the shell's orientation that complements the direction given by the 3-axis magnetometer. The two sources of information are combined into an attitude estimate by a specific nonlinear observer. Experimental results obtained with a gyrostabilized supersonic 155 mm shell are presented.

Keywords: exterior ballistics, flight dynamics, frequency detection, attitude estimation, inertial sensors, embedded sensors

Introduction

The article proposes a method to estimate the attitude of an artillery shell in free flight. Attitude estimation is essential for «*smart shells*», a.k.a. «*guided ammunition*», pictured in Fig. 1, which are capable of achieving various tasks such as in-flight retargeting and range optimization, as illustrated in Fig. 2. To perform these tasks, smart shells are equipped with pyrotechnical thrusters (the thruster is presented in Fig. 3 and its retargeting effects are illustrated in Fig. 4). When reorientation of the shell is desired, the thruster ignition time is precisely chosen to obtain the desired effect, according to the desired reorientation and the current attitude.

Attitude estimation using sensors attached to a rigid body is a vast subject. Classically, following the formulation of the Wahba problem [1], two vector measurements, usually assumed to be obtained using accelerometers and magnetometers, are used to algebraically and unambiguously reconstruct the attitude. The largely documented methods to solve Wahba problem (see [2, 3, 4]) have been improved in many applications with multi-sensor data fusion; adding a rate gyro to the set of sensors, most often using Kalman filtering (see, e.g., [5]); or, more recently, complementary filtering as in [6, 7, 8]. When employed, the rate gyro brings robustness to vector-measurement failures and provides dynamic responsiveness to the estimate. Numerous experiments and works [9, 10, 11, 12, 13, 14, 15, 16, 17, 18] offer comparisons of methods implementing such attitude-estimation techniques for various aerospace, mechatronics and robotics systems.

However, the application of such approaches to artillery shells is not straightforward. On the hard-

*Corresponding author. Conflict of interest - none declared
Email addresses: aurelien.fiot@mines-paristech.fr (Aurélien Fiot), Sebastien.changey@isl.eu> (Sébastien Changey), nicolas.petit@mines-paristech.fr (Nicolas Petit)

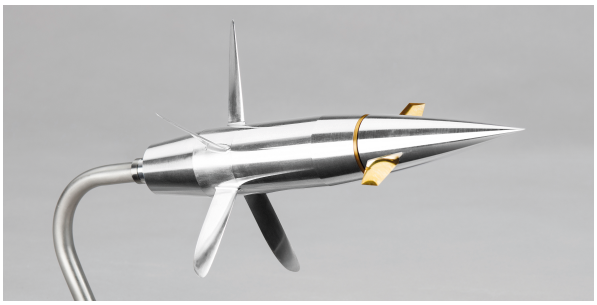

Figure 1: ISL guided long range projectile.

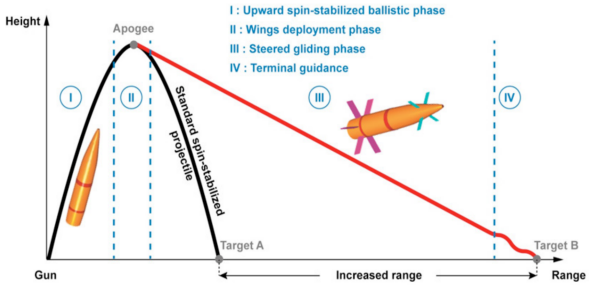

Figure 2: Typical ballistic flight phases for smart artillery shells. (ISL)

ware side, all the inertial sensors cited above reveal troublesome. The rate gyro is too fragile to survive the stress of gunshot and can not be employed. Induction effects due to the spin rates strongly perturb the magnetometers [19]. Finally, a main challenge concerns accelerometers which measure proper acceleration. In free fall, accelerometers do not accurately measure gravity's direction. This well-known fact seems to discard the attitude estimation techniques cited above in the domain of artillery shell applications.

Fortunately, it is possible to circumvent this intrinsic flaw by employing the accelerometers not to measure the direction of gravity but to estimate the shell velocity w.r.t. the air. During the whole ballistic flight, accelerometers measure aerodynamic forces. These forces generate an epicyclic motion whose frequencies are directly related to the shell's velocity w.r.t. the air [20]. Once detected, the frequencies can serve to estimate the velocity through analytical formulas stemming from an aerodynamic model. This estimate can serve to evaluate the pitch angle of the rigid body. This last piece of information complements the measurement from the magnetometer and allows one to determine the complete attitude of the shell.

The main methodological novelties of the article are this frequency-based use of the accelerometers and a specific complementary filter providing a complete estimate of the shell's attitude. The main contribution is a comprehensive presentation of the methodology along with practical implementation details and experimental results. The paper is organized as follows. Section 1 presents the notation and the problem statement. Section 2 describes the epicyclic motion. Section 3 details the onboard instrumentation used for the application on a 155 mm supersonic gyrostabilized artillery shell and lists several practical challenges and solutions to obtain relevant data from the sensors. Section 4 presents the employed frequency determination technique. Section 5 reports the method used to estimate the translational velocity and deduce the pitch angle. Finally, Section 6 presents the novel complementary filter, its convergence properties, and experimental results of attitude determination.

1. Notation and problem statement

1.1. Reference frames and six-degrees-of-freedom description

The local frame of reference is the «*North-East-Down*» (NED) frame rotated so that its first vector points toward the direction of the shot. The shell is modeled as a Six-Degrees-of-Freedom (6-DOF) rigid body. Table 1 lists relevant notations.

The orientation of the rigid body is defined by a set of three Tait-Bryan angles (here «*ZYX*» angles are chosen and the spin is defined as the rotation about the shell's axis of least inertia). Besides the local (inertial) frame L and the body frame B, a third frame is considered. The «*wind velocity frame*» is noted W. It is defined from B using the velocity of the shell w.r.t. the airflow, the norm of which is v. Classically, the three angles define the attitude matrix

$$R \triangleq R_{\Psi,e_3} R_{\Theta,e_2} R_{\Phi,e_1}$$

where e_1, e_2, e_3 are a direct orthonormal basis of L. The attack angle α and the sideslip angle β are defined by the transition matrix $R_{-\alpha,e_2} R_{\beta,e_3}$ from B to W.

1.2. Problem statement

The problem under consideration is to estimate the attitude matrix R using the measurements from

Figure 3: ISL pyrotechnical thruster. Top: close-up view during thrust. Middle: integration in a 155 mm shell. Bottom: the thruster.

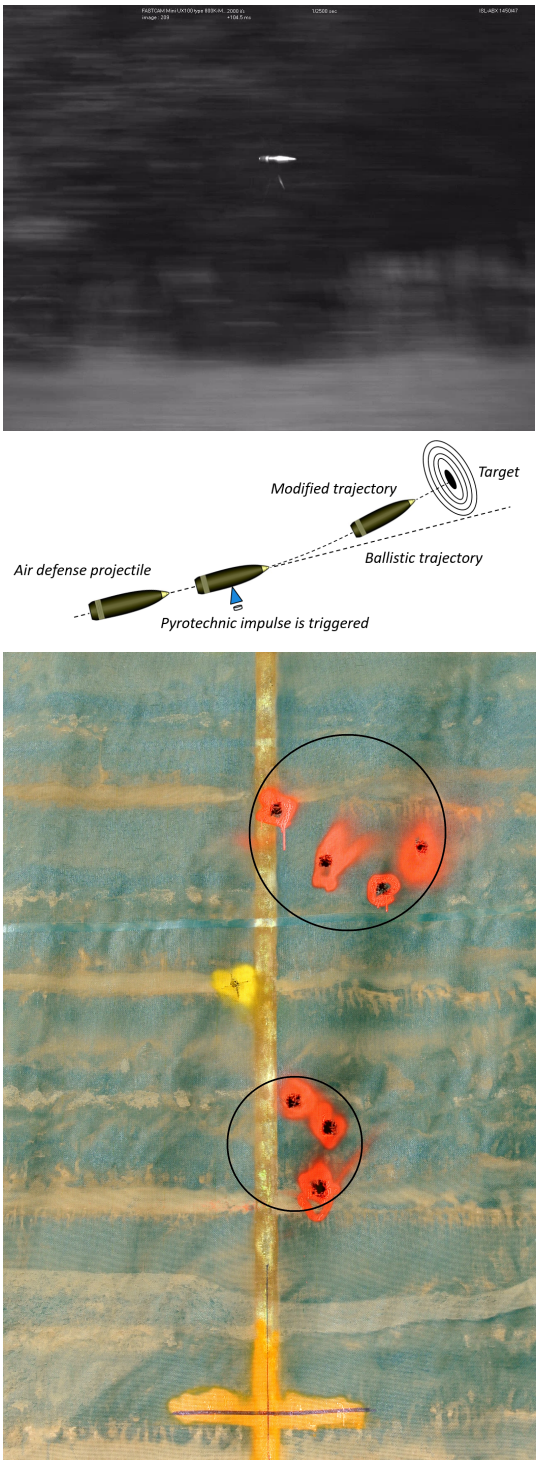

Figure 4: Top: ISL pyrotechnical thruster in action. Middle: Reorientation of the ballistic trajectory using the pyrotechnic impulse. Bottom: Impact points of ballistics shots (below), and reoriented shots (top), an overall translation of 80 cm is obtained at the endpoint of a 150 m flight.

a strapdown 3-axis magnetometer $Y_{mag} \triangleq R^T b_0$ (where b_0 is the known value of the local Earth magnetic field) and Y_{acc} the measurements from a strapdown 3-axis accelerometer.

To understand which information can be deduced from Y_{acc}, it is necessary to study the rotational dynamics of the rigid body. This is done next.

2. Shell rotational dynamics

Euler's equation of rotation of a rigid body subjected to external aerodynamic moments are Eqs. (1) to (3). They account for Magnus $\mathcal{M}$, overturning $\mathcal{O}$, rolling $\mathcal{D}_p$, pitch damping, and roll damping $\mathcal{D}$ moments

$$I_l \frac{d}{dt} p = -\mathcal{D}_p(h)\, v\, p \tag{1}$$

$$I_t \frac{d}{dt} q = (I_l - I_t) p\, r + \mathcal{M}(h)\, v\, \beta + \mathcal{O}(h)\, v^2\, \alpha - \mathcal{D}(h)\, v\, q \tag{2}$$

$$I_t \frac{d}{dt} r = (I_l - I_t) p\, q + \mathcal{M}(h)\ v\, \alpha - \mathcal{O}(h)\, v^2\, \beta - \mathcal{D}(h)\, v\, r \tag{3}$$

The bilinear term $q\,r$ in Eq. (1) has vanished due to the symmetric nature of the shell.

2.1. Complex-domain oscillator

As shown in the early work of [21], the reaction of the shell to aerodynamic forces and moments has a relatively simple form when its axis of symmetry, its axis of rotation and the direction of motion of its center of mass though the air all coincide. This is precisely the case for the shells studied here. Several steps of calculus and careful first-order approximations [1], see [20, Chapter 10], allow one to derive the equation governing the Pitching and Yawing motion of the rotationally symmetric projectile. In detail, by introducing rotated incidence angles $\alpha_2 \triangleq \sin(pt)\,\alpha - \cos(pt)\,\beta$, $\beta_2 \triangleq -\cos(pt)\,\alpha - \sin(pt)\,\beta$ and considering the *complex yaw* $\xi \triangleq \alpha_2 + i\beta_2$ one obtains the following complex-valued ordinary differential equation

$$\frac{d^2}{dt^2}\xi + v(H - iP)\frac{d}{dt}\xi - v^2(M + iPT)\xi = -iPG \tag{4}$$

[1] during the whole flight (typically lasting less than 45 s for ballistic flight and less than 2 s for flat-fire) the spin rate remains very high, and the angles of attitude w.r.t. the wind frame remain small. Therefore, it is possible to study the attitude dynamics, and, in turn, the translational dynamics, under the assumption of small-angles.

where H, P, M, T are functions of the aerodynamic coefficients of the shell, and G contains the roll angle.

v	Norm of velocity of the shell w.r.t. the airflow
R	Attitude matrix of the shell
Ψ, Θ, Φ	(Yaw, Pitch, roll) Tait-Bryan angles
α, β, θ	Attack, sideslip and slope angle
$\Omega = (p, q, r)$	Angular velocity of the shell w.r.t. the local frame expressed in the body frame
p	Spin rate of the shell
q, r	transverse components of Ω
I_l, I_t	Longitudinal and transverse moment of inertia
$h > 0$	Altitude of the shell

Table 1: Nomenclature.

Eq. (4) is fully described in [20, 22]. It is central in this article. It has been established by several authors, under various forms, which are all equivalent, see [23, 24, 25, 26], among others. It is a linear, second-order differential equation with slowly-varying complex coefficients. Solving Eq. (4) for a short time horizon reveals that the pitching and yawing motion of the shell consists of two oscillation modes so that the complex yaw ξ follows an *epicyclic motion* in the complex plane, i.e., a motion of the form

$$\xi(t) = A_n e^{i\omega_n t} + A_p e^{i\omega_p t} + A_0 \tag{5}$$

where ω_n and $\omega_p << \omega_n$ are «*nutation*» and «*precession*» angular frequencies, respectively. The epicyclic motion is pictured in Fig. 5. The nutation and precession frequencies have symmetrical expressions

$$\omega_n = p\frac{I_l}{2I_t} + \frac{v}{2}(P_1^2 + P_2^2)^{\frac{1}{4}} \cos\left[\frac{1}{2}\arctan\left(\frac{P_2}{P_1}\right)\right] \tag{6}$$

$$\omega_p = p\frac{I_l}{2I_t} - \frac{v}{2}(P_1^2 + P_2^2)^{\frac{1}{4}} \cos\left[\frac{1}{2}\arctan\left(\frac{P_2}{P_1}\right)\right] \tag{7}$$

where analytic expressions of P_1, P_2 in terms of the aerodynamics parameters of the shell and the variables (v, h, p) are given in [22]. The «*body-attached*»

incidence angles are given by

$$\alpha + i\beta = -i\left(A_n e^{i(p-\omega_n)t} + A_p e^{i(p-\omega_p)t} + A_0 e^{ipt}\right) \tag{8}$$

2.2. Frequency content of the 3-axis accelerometer signals

The angular frequencies appearing in Eq. (8) are observed in the aerodynamics forces, and therefore, in the 3-axis accelerometer signals.

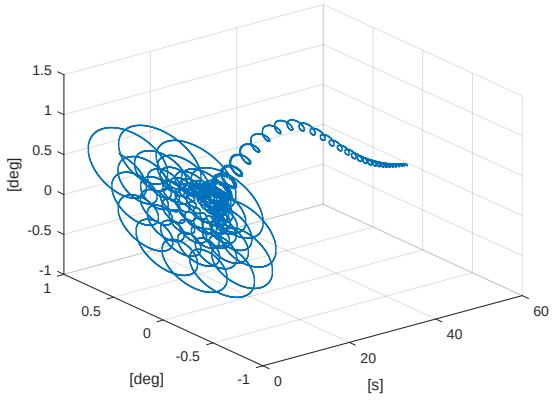

Figure 5: Epicyclic motion of the shell during a typical flight; locus of the complex yaw ξ from Eq. (5) [simulation results].

Fig. 6 reports the theoretical values of the angular frequencies at stake throughout a typical ballistic flight. These plots are obtained through the analytic expressions of the frequencies and a detailed aerodynamic model. As appears in Eqs. (6) and (7), the frequencies of the epicyclic motion carry information on the velocity v. This property is instrumental in the study conducted in this article.

3. Onboard sensors

The strapdown sensors embedded into the shells (see Fig. 7) consist of a 3-axis accelerometer and a 3-axis magnetometer. The sensors data is collected and radio transmitted during the flight using the shell's cone as a monopole antenna. Up to 2 megabytes per second of data can be streamed with a low level of losses[2]. All sensors are synchronous and sampled at the same rate (8064 Hz). The embedded system is pictured in Fig. 7.

[2]as will be visible when treating data, some outliers appear, especially at the end of the flight when the shell is the farthest from the receiving antenna.

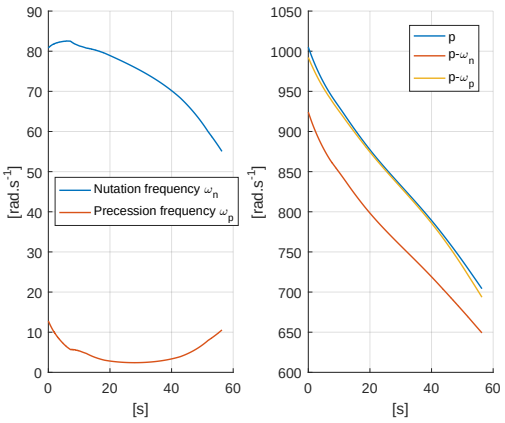

Figure 6: Theoretical frequencies of the epicyclic motion $\omega_p < \omega_n$ (left) and theoretical frequencies $p-\omega_n < p-\omega_p < p$ contained in the signal from any of the transverse accelerometers (right) [simulation data].

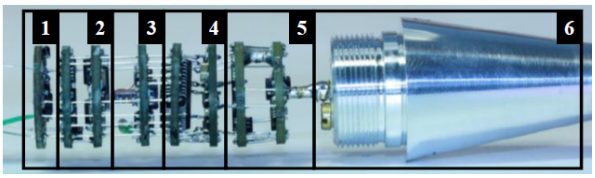

Figure 7: Embedded Instrumentation, from [19], used for the experiments studied in this article. 1: Power supply unit, 2: 3-axis magnetometer, 3: 3-axis accelerometer, 4: CPU (for signal conditioning), 5: RF Transmitter, 6: Monopole Antenna.

Below, several detrimental effects impacting the sensors are discussed along with corresponding mitigation means.

3.1. Eddy currents

Once embedded into the shell, the 3-axis magnetometer is heavily corrupted by an induction effect created by the high spin rate of the electrically conductive shell. The rotation around its main axis is the root cause of eddy currents. Fortunately, these effects can be mitigated by suppressing the known induction response to a given spin rate, previously modeled and measured on a testbed [19]. Once this compensation is achieved, the residual induction effects are negligible. Accurate compensation requires knowing the spin rate, the estimation of which is explained in Section 4.1.

3.2. Misalignment

The sensor suite is never perfectly aligned with the body axes. In practice, a small rotation ex-

ists between the sensors frame and the body frame. This rotation results in a malicious modulation visible in the signals. For example, in theory, there should be no oscillations at the spin rate frequency on the longitudinal magnetometer, but it is clearly seen in raw measurements. Interestingly, this fact suggests a procedure to address the misalignment. An additional rotation is applied to the measurements. The rotation is chosen so that it minimizes the variance of the longitudinal component. Fig. 8 illustrates the benefits of this misalignment compensation procedure, and the reduction of the variance of the signal.

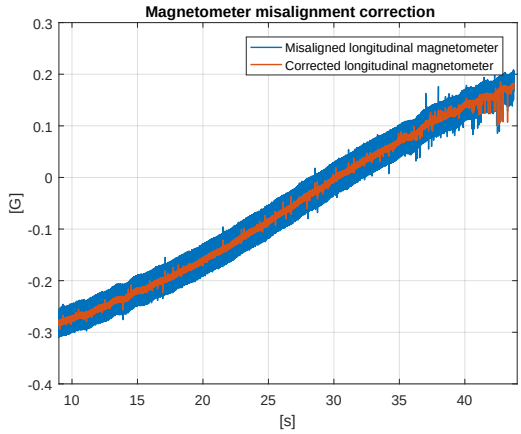

Figure 8: Compensation of the longitudinal magnetometer misalignment. A rotation of approximately 4 deg was employed. [experimental data].

3.3. Fictitious forces

The accelerometers are disturbed by fictitious forces. Indeed, due to the high values of the spin rate under consideration (above 900 rad/s), even small residual misalignments (see Section 3.2) or lateral shift of the sensors from the shell main axis induce substantial fictitious forces which directly corrupt the readings of the 3-axis accelerometer. Sensors are located in the nose of the shell, approx. 20 cm away from the center of mass. Interestingly, this is harmless for the frequency-based methodology because the dominant fictitious forces share the same frequency content as the valuable signals for the reasons detailed below.

In detail, let Y_{acc0} denote the proper acceleration measured at the center of mass of the shell, then the proper acceleration occurring at a location shifted by a vector d is

$$Y_{acc} = Y_{acc0} + \Omega \times (\Omega \times d) + \frac{d\Omega}{dt} \times d \qquad (9)$$

The longitudinal component of d is large. Despite significant efforts in the mechanical design and construction phases, the sensors are not located right onto the shell symmetry axis. A small but non-negligible *transverse* component appears in d. The high spin rate has a tremendous effect in Eq. (9) even for small such transverse shift. This effect is visible in Fig. 9 which compares experimental signals and their theoretical counterparts. According to Eq. (9), the factors that can cause fictitious forces are (only their orders of magnitude are reported): Long. shift $d_1 = 10^{-1}$, Trans. shift $d_2 = 10^{-4}$, $d_3 = 10^{-4}$ (m), $p = 10^3$, $q = 10^1$, $r = 10^1$ (rad.s^{-1}). In turn, the various disturbance terms appearing in the expanded form of Eq. (9) are listed by descending order of magnitude in Table 2. The «*frequency content*» column in Table 2 describes the oscillating contribution of each term (q and r obeying Eq. (2) and Eq. (3), respectively, and p being almost linearly damped according to Eq. (1)). It is worth mentioning that the term $d_1\,(p\,q + \frac{d}{dt}r)$ is actually much smaller than its constituting factors because, as can be seen in the last part of the rotational dynamics Eq. (3), one has that $I_t >> I_l$ implies that $\frac{d}{dt}r \approx -p\,q$. This term is not negligible but it has the same frequency content as Y_{acc0}. Then, it appears that the dominant fictitious force is $-d_2\,p^2$ and that it acts as a (slowly drifting) bias on the 3-axis accelerometer. This drifting bias is visible in Fig. 9 (bottom-left and -right plots). Interestingly, the bias is substantial, but it does not alter the frequency content of the 3-axis accelerometer signals.

4. Frequency-based estimation of the translational velocity

4.1. Estimation of the spin rate

As seen in Eq. (1), the spin rate p has autonomous dynamics with almost linear damping. Various methods can be employed to estimate the (vector) angular velocity without rate gyro, e.g., [27, 28, 29, 30, 31, 32]). Here, a simpler approach can be used because the angular velocity (p, q, r) is actually close to (p, 0, 0). To estimate p, the complex argument method presented in Appendix

Expression	Range of value	Frequency content
Y_{acc0}	$10^1 \rightarrow 10^0$	$p, p-\omega_n, p-\omega_p$
$-d_2\, p^2$	10^2	None
$d_1(\, p\, q + \frac{d}{dt} r)$	$10^1 \rightarrow 10^0$	p, $p-\omega_n$, $p-\omega_p$
$d_3\, q\, r$	10^{-2}	Interference[3] of p, $p-\omega_n$, $p-\omega_p$
$-d_2\, r^2$	10^{-2}	Interference of p, $p-\omega_n$, $p-\omega_p$
$-d_3\, \frac{d}{dt} p$	10^{-3}	None

Table 2: Signal at the center of mass and fictitious forces in one transverse accelerometer. Values in $\mathrm{m.s}^{-2}$.

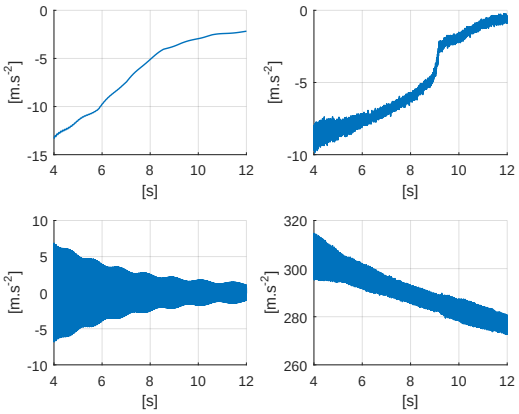

Figure 9: Values of longitudinal and transverse 3-axis accelerometer signals: simulation (left), experimental (right).

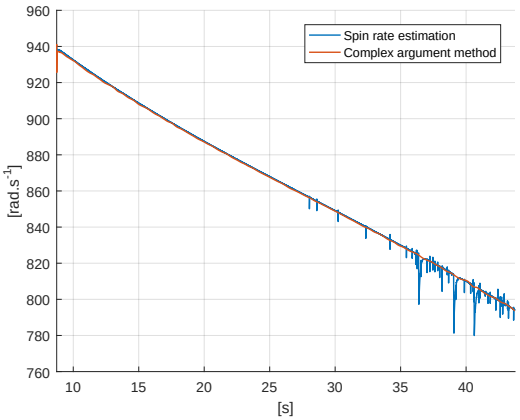

Figure 10: Estimation of spin rate [experimental results].

is applied. Further, to filter any outlier, an extended Kalman filter with a model $\ddot{p} = 0$ is employed. Fig. 10 reports estimates obtained from experimental signals.

4.2. Application of classic frequency detection techniques

The expressions in Eqs. (6) and (7) suggest that several frequencies can be used as sources to estimate the velocity. It is advised to focus on $\omega_n >> \omega_p$ for two reasons. It is the easiest to measure over short time windows (because a larger number of its periods are contained in a given time window), and it is also the easiest to distinguish from the spin rate in the accelerometer signal (see Fig. 6-right).

A common practice to estimate frequencies in a multisinusoidal signal is to use Fast Fourier Transform (FFT) over sliding windows. This technique is at the heart of the popular *periodogram* technique [33]. The sensor signals contain the frequency $p - \omega_n$. However, the main interest lies in detecting ω_n. A solution is to treat the signal directly, detect $p - \omega_n$ as one of the peaks of the FFT, and deduce ω_n by subtracting the known value of p (see Section 4.1). This calculus can be done but is not the best option because, as illustrated in Fig. 6, the frequencies $p - \omega_n < p - \omega_p < p$ are relatively close. Consequently, the accuracy of the estimate obtained by subtraction can be poor. Instead, a helpful alternative is to process the signal's envelope instead of the signal itself. The computation of the envelope can be performed using an envelope-follower filter or the Hilbert transform. A Han window can be applied to the envelope to minimize the aliasing effect and leakage in the FFT (leakage is mostly due to the number of cycles in the time window being fractional). In all cases, zero-padding shall be applied to improve the resolution of the FFT. Then, the frequency estimate is found as one of the peaks of the FFT. For improved accuracy, the peak can be determined as the maximum of a local polynomial fit of neighboring values of the FFT. These methods have all been tested, see [22]. They produce good results on simulation data, but they

are outperformed when employed on experimental data by the method presented next.

4.3. Subspace method for frequency estimation

For a sum of sinusoids covered in noise, the *subspace* methods are appealing. They rely on the spectral decomposition of the autocorrelation matrix. Historically, the first subspace method was introduced by Pisarenko [34]. It is now seen as a particular case of the MUSIC method introduced by Schmidt [35]. There exist other subspace methods such as minimum norm algorithm or eigenvector method [36]. They behave similarly on our system. Consider a signal

$$s(t) = \sum_{k=1}^{p} \alpha_k e^{i(\omega_k t + \varphi_k)} + n(t)$$

where $n(t)$ is an additive noise (real white noise with zero mean and variance σ^2, after sampling), $(\omega_k)_{k=1,...,p}$ are p *unknown* frequencies to be determined, $(\alpha_k)_{k=1,...,p}$ are unknown constant amplitudes and $(\varphi_k)_{k=1,...,p}$ are unknown phases (independent random variables uniformly distributed over $[0, 2\pi]$). To determine the frequencies, subspaces methods rely on the spectral decomposition of the autocorrelation matrix estimated from samples $s[0]$, $s[1]$, ..., $s[N-1]$.

The autocorrelation matrix of size $m > p$ of the signal is defined as $C = E[y(t)y^*(t)] \in \mathbb{C}^{m\times m}$ with $y(t) = \big(s(t)\cdots s(t+m-1)\big)^T$, where * designate the conjugate transpose. Several lines of calculus show, see [37], that

$$C = APA^* + \sigma^2 I_m \tag{10}$$

where $A = \begin{pmatrix} a(\omega_1) & \cdots & a(\omega_p)\end{pmatrix} \in \mathbb{C}^{m\times p}$, $a(\omega) \triangleq \big(1, e^{i\omega}, \ldots, e^{i\omega(m-1)}\big)^T$ and $P = \mathrm{diag}(\alpha_1^2, ..., \alpha_p^2)$. Then, it follows that the eigenvalues of C are all real and satisfy $\lambda_1 \geq \lambda_2 \geq ... \geq \lambda_p > \lambda_{p+1} = \lambda_{p+2} = ... = \lambda_m = \sigma^2$. Note $S \triangleq \begin{pmatrix} s_1 & \cdots & s_p\end{pmatrix}$ the orthonormal eigenvectors of C associated to $\{\lambda_1, ..., \lambda_p\}$ and $G \triangleq \begin{pmatrix} g_1 & \cdots & g_{m-p}\end{pmatrix}$ the orthonormal eigenvectors associated to $\{\lambda_{p+1}, ..., \lambda_m\}$. Then, one has

$$a^*(\omega_i)GG^*a(\omega_i) = 0 \text{ for } i \in \{1, ..., p\} \tag{11}$$

A result worth mentioning is that $G^*a(\omega) \neq 0$ for $\omega \notin (\omega_k)_{k\in\{1,...,p\}}$. The idea behind subspace methods is to use this property to build a frequency-discriminating function having local maxima at $(\omega_k)_{k=1,...,p}$. The (frequency-discriminating) function used in the MUSIC algorithm (see [38] for details) is :

$$h_{MU}(\omega) = \frac{1}{\sum_{i=1}^{m-p} \|g_i^* a(\omega)\|^2} = \frac{1}{a^*(\omega)GG^*a(\omega)} \tag{12}$$

Constructing this function requires building an estimation of G from signal samples, which in turn calls for an estimation of the autocorrelation matrix. This is readily done as the empirical autocorrelation matrix $\hat{R} = \frac{1}{M}\sum_{n=0}^{M-1} y[n]y^*[n]$ is an unbiased estimator of R, with $M = N - m + 1$.

Gathering all the ingredients above, one can formulate a streamlined subspace algorithm: Ⓐ compute $\hat{C} = \frac{1}{M}\sum_{n=0}^{M-1} y[n]y^*[n]$, Ⓑ compute $\hat{S}$ with the p largest eigenvalues eigenvectors of $\hat{C}$, Ⓒ determine[4] the p dominant peaks of $\hat{h}_{MU}(\omega) = \frac{1}{a^*(\omega)(I-\hat{S}\hat{S}^*)a(\omega)}$. These are the frequency estimates $(\hat{\omega}_k)_{k=1,...,p}$.

4.4. Application to the transverse accelerometer signal

The vectorspace algorithm described above is implemented to treat the transverse accelerometer signal. Analysis of the successive maxima of the frequency discriminating function gives the value of $p - \omega_n$. Once combined with the estimation of p from Section 4.1, this gives an estimate of ω_n.

During the flight, the Signal-to-Noise Ratio (SNR) decreases because the epicyclic motion pictured in Fig. 5 decays. The SNR of the 1-axis transverse accelerometer (estimated from filtering) is reported in Fig. 11a. Also, data gradually gets more corrupted when the shell gets further away from the receiving antenna. Among all available data, a time window [8.75, 43.5] is selected. Over this window, approx. 4.6% of data points are corrupted. The frequency estimate is of good quality at the beginning of the sequence and gets noisier at later stages, see Fig. 11b. The estimates can be fitted to a fourth-order polynomial in the time variable. The estimate is debiased to match the model predictions at the end of the window.

5. Velocity and pitch estimation

5.1. Reference velocity

The reference serving as ground-truth is the velocity w.r.t. the local frame. It is measured on

[4] or $\hat{h}_{MU}(\omega) = \frac{1}{a^*(\omega)\hat{G}\hat{G}^*a(\omega)}$ because $\hat{G}\hat{G}^* = I - \hat{S}\hat{S}^*$

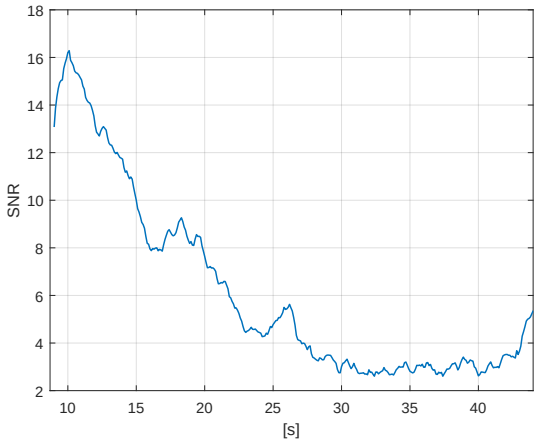

(a) Signal/noise ratio. $10 \cdot \log_{10}$ SNR is reported.

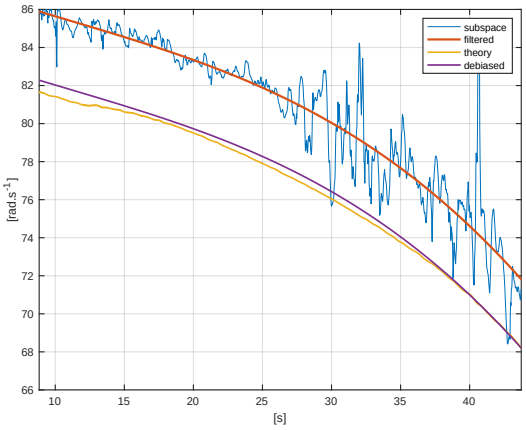

(b) Frequency detection against theoretical frequencies.

Figure 11: Experiments on frequency detection.

the shooting range with a ground-based position radar. The shell reaches Mach 1 at an instant that is easily detected on the longitudinal accelerometer, which features a sudden signal jump. Comparing the value of 317.8 m/s obtained from the frequency estimate through the velocity model with Mach 1 (332 m/s) [5], one can deduce that the velocity estimate is biased (at this particular instant) by ≈ 13.2 m/s. Applying the inverse of the velocity model, one deduces that the frequency estimate is biased by ≈ 2 Hz. Accordingly, a constant bias correction is applied over the whole time interval. The result of this bias correction is reported in Fig. 11b.

[5] assuming the altitude is equal to the reference altitude for such a 155 mm fired at nominal speed, which is corroborated by the ground-based position radar measurements.

5.2. Design of an observer for the velocity from frequency measurements

A state observer can be used to estimate the translational velocity. It uses the open-loop dynamics of the translation velocity, which includes h and θ dependent terms that can be replaced with reference histories provided that they are well synchronized (which is done by detecting gun fire from any of the embedded signal, e.g., any of the accelerometers). The dynamics rewrite as a single-state time-varying nonlinear dynamics, with a nonlinear measurement equation stemming from Eq. (6)

$$\frac{d}{dt}v(t) \triangleq f(v,t), \quad y(t) \triangleq g(v,t) \tag{13}$$

Observer design for this nonlinear dynamics Eq. (13) seems, at first, a routine problem. The main difficulty here is that g in Eq. (13) is not one-to-one. The behavior of aerodynamic drag-induced effects near Mach 1.0 implies that for any given t, the mapping $v \mapsto \frac{\partial g}{\partial v}(v,t)$ has a fixed number N of zeros (at least 2). These zeros represent time-varying critical velocities. Although f becomes steep near these points, it remains monotonic w.r.t. v at all times. Some analytical study reveals that $\frac{\partial C_D}{\partial v}$ remains small enough, for all v and t of interest in this study, so that $\frac{\partial f}{\partial v}$ stays strictly negative and bounded [22]. Therefore, the mapping f is a contraction in the sense of [39]. An observer is quite easy to design. To speed up the convergence, one can make active usage of the measurement y using a gain having the same sign as $\frac{\partial g}{\partial v}$. Following common practice, see e.g. [40, 41, 42] and references therein, near the critical velocities, the gain is set to zero. This defines a gain-switching observer where the gain is a function of the current estimate. Exponential convergence analysis is given in [22]. The obtained results are reported in Fig. 12a.

5.3. Slope and pitch estimation experimental results

The orientation of the shell velocity defines the slope angle, which is equal to the pitch angle when the total angle of attack is zero. This assumption is true on average (except near apogee) for typical flights. The mismatch is bounded by the total angle of attack of the shell, which commonly does not exceed a few degrees, and exponentially decreases during the flight. To estimate θ from the estimate of the translational velocity v, the following output

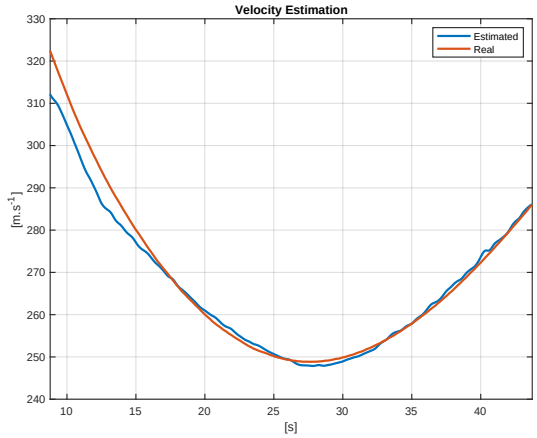

(a) Velocity.

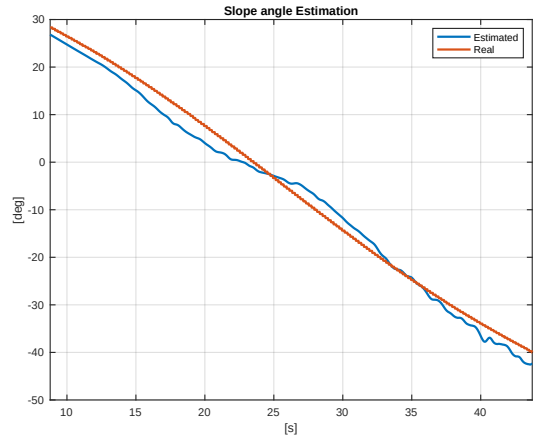

(b) Slope angle.

Figure 12: Velocity and slope angle estimation [experimental results].

injection observer is considered

$$\begin{cases} \frac{d}{dt}\hat{h} &= v\sin\hat{\theta} + l_1(v-\hat{v}), \\ \frac{d}{dt}\hat{\theta} &= \omega + l_2(v-\hat{v}) \\ \frac{d}{dt}\hat{\omega} &= l_3(v-\hat{v}), \\ \frac{d}{dt}\hat{v} &= -D(\hat{h},v) - g\sin\hat{\theta} + l_4(v-\hat{v}) \end{cases} \tag{14}$$

A procedure can be established to determine constant gains l_1, l_2, l_3, l_4 that provide exponential convergence over the whole flight. Advantageously, if computational load is not a concern, an EKF can be preferred, see [22] for details.

5.4. Experimental results

When using a ground-based position radar measurement of the velocity, it has been established that the slope angle can be estimated with a residual error below 2 deg [22], stressing the validity of the model. When the velocity estimation is used instead, the slope estimation error has slightly more variance as reported in Fig. 12b.

6. Attitude observer

A data fusion between the single direction measurements and the angle estimate is now performed to reconstruct the attitude.

6.1. A quaternion representation of the problem

The set of unit quaternions is denoted $\mathbb{Q} = \{q = (s, v \triangleq \mathrm{dir}(q)) \in \mathbb{R}\times\mathbb{R}^3, |q| = 1\}$. The quaternion product

$$q_1 \otimes q_2 = \begin{pmatrix} s_1 s_2 - v_1^T v_2 \\ s_1 v_2 + s_2 v_1 + v_1 \times v_2 \end{pmatrix}$$

has (1, 0, 0, 0) as identity element. The group of unit quaternions is homomorphic to the group SO_3 of rotations about the origin of $\mathbb{R}^3$, via the mapping

$$F(q) := I_3 + 2s[v_\times] + 2[v_\times]^2 \tag{15}$$

where $[v_\times]$ is the skew-symmetric matrix corresponding to the cross product in $\mathbb{R}^3$, $v \times \cdot$. Conversely, for any angle θ and any direction a, the quaternion associated with the rotation $R = \exp(\theta\, a_\times)$ is $q_{\theta,a} = \big(\cos(\frac{\theta}{2}), \sin(\frac{\theta}{2})a\big)$. The pure quaternion $\boldsymbol{p}(\Omega) \triangleq (0, \Omega)$ is such that the rotation kinematics writes $\frac{d}{dt}\hat{q} = \frac{1}{2}\hat{q} \otimes \boldsymbol{p}(\Omega)$.

6.2. Recalls on attitude complementary filter

For now, consider a rigid body equipped with two embedded vector sensors producing measurements

$$v_i = R^T \mathring{v}_i, \quad i = 1{,}2 \tag{16}$$

where $\mathring{v}_1, \mathring{v}_2$ are two constant (unit) vectors expressed in the inertial frame. Assuming that they are non-colinear, i.e., $\mathring{v}_1^T \mathring{v}_2 \neq 0$, it is possible to estimate R using the following state observer (Explicit complementary filter [7])

$$\begin{cases} \frac{d}{dt}\hat{R} = \hat{R}\Big([(\Omega^y - \hat{b})_\times] + k_P[\sigma_\times]\Big) \\ \frac{d}{dt}\hat{b} = -k_I\sigma \\ \quad \sigma = k_1 v_1 \times (\hat{R}^T\mathring{v}_1) + k_2 v_2 \times (\hat{R}^T\mathring{v}_2) \end{cases} \tag{17}$$

where $\Omega^y = \Omega + b$ is the measurement from an embedded gyro assumed to be corrupted with a

constant bias b, and where k_I, k_P, k_1 and k_2 are constant positive tuning parameters. Commonly, σ is referred to as the innovation vector. It is null when the measurement matches the prediction. This observer has three unstable equilibria $(\hat{R}_{\star i}, \hat{b}_{\star i}) \triangleq (U_0 D_i U_0^T R, b), \quad i = 1, 2, 3$ where $D_1 = \mathrm{diag}(1, -1, -1)$, $D_2 = \mathrm{diag}(-1,1,-1)$ and $D_3 = \mathrm{diag}(-1, -1,1)$, and $U_0 \in SO(3)$ such that $M_0 \triangleq \sum_{i=1}^{2} k_i \mathring{v}_i \mathring{v}_i^T = U_0 \Lambda U_0^T$ with Λ a diagonal matrix. Its error $(\tilde{R}(t), \tilde{b}(t))$ is locally exponentially stable to $(I, 0)$ and for almost all initial conditions $(\hat{R}_0, \hat{b}_0) \neq (\hat{R}_{\star i}^T R, b)$ the trajectory $(\hat{R}(t), \hat{b}(t))$ converges to the trajectory $(R(t), b)$.

6.3. Partial convergence using a single direction

The complementary filter above can deal with an arbitrary number of direction measurements. However, when employed with only a single direction, the filter converges to a continuous set that is *not* restricted to the actual attitude. Some partial convergence results can be still be adapted from [6] and will prove to be instrumental in the proposed adaptation.

Consider only $Y_{mag} = R^T b_0$ the measurement from the 3-axis magnetometer, and $\hat{q}$ the unit quaternions representation of $\hat{R}$. An equivalent formulation of the attitude estimation equation is, (leaving out the bias compensation)

$$\frac{d}{dt}\hat{q} = \frac{1}{2}\hat{q} \otimes \boldsymbol{p}\left(\omega + k_p (Y_{mag} \times (\hat{q}^{-1} b_0 \, \hat{q}))\right) \quad (18)$$

The innovation vector is

$$\sigma \triangleq Y_{mag} \times (\hat{q}^{-1} b_0 \, \hat{q}) = (q^{-1} b_0 \, q) \times (\hat{q}^{-1} b_0 \, \hat{q}) \quad (19)$$

For any quaternions q_1, q_2 in $\mathbb{Q}$, the following errors are considered

$$\delta(q_1, q_2) \triangleq 2 \arccos\left((q_2 \otimes q_1^{-1})_1\right) \quad (20)$$

$$u(q_1, q_2) \triangleq \begin{cases} \frac{\mathrm{dir}(q_2 \otimes q_1^{-1})}{\sin \frac{\delta(q_1, q_2)}{2}} \text{ if } \delta(q_1, q_2) \neq 0 \\ b_0 \text{ otherwise} \end{cases} \quad (21)$$

where $(.)_1$ is the first component of its argument and dir is the last three components of its argument.

The convergence analysis provided in [6] states that, in almost all cases[6],

$$\lim_{t \to +\infty} \sigma(t) = 0 \quad (22)$$

[6] except for a set having zero-measure.

Some lines of calculus [22] show that Eq. (22) implies that one has, as $t \to +\infty$, $(I + 2\delta(q, \hat{q})[u(q, \hat{q})_\times] + 2[u(q, \hat{q})_\times]^2) b_0 \to b_0$. This property can be analysed further, to show that

$$\lim_{t \to +\infty} u(q(t), \hat{q}(t)) = b_0 \quad (23)$$

This last equation reveals that $\hat{q}$ asymptotically approaches a set containing the true attitude quaternion q. The set is not limited to this desirable value, unfortunately. The set contains all rotations about b_0 starting from the true rotation.

6.4. Proposed observer

To account for the available pitch information, one can consider a modified version of the complementary filter with a second equation taking the form of a gradient-based integrator, using a comparison of the actual pitch and the predicted one. The gain employs a saturating linearizing gain $\kappa : x \mapsto \sqrt{1 + x^2}/\tanh(x)$. The prediction is performed based on the updated quaternion $\bar{q}$ obtained by a rotation of the filtered quaternion $\hat{q}$, the rotation being of magnitude defined by the state χ of the gradient-based integrator. The input of the observer are the innovation σ computed using the 3-axis magnetometer measurement according to Eq. (19), the angular rate Ω (here supposed to be known, which will be replaced in applications by the estimate $(p, 0, 0)$ discussed in Section 4.1), and the pitch angle under the form $T(q) \triangleq q_1 q_3 - q_2 q_4 = \frac{1}{2}\sin(\Theta)$. The output of the attitude observer is $\bar{q}$.

$$\begin{cases} \dfrac{d}{dt}\hat{q} = \dfrac{1}{2}\hat{q} \otimes \boldsymbol{p}\left(\Omega + k_p \sigma\right), \quad \sigma \triangleq Y_{mag} \times (\hat{q}^{-1} b_0 \, \hat{q}) \\ \dfrac{d}{dt}\chi = k_c \dfrac{T(q) - T(\bar{q})}{\kappa\left(\nabla T(\bar{q})^T (\boldsymbol{p}(b_0) \otimes \bar{q})\right)} \\ \bar{q} = \left(\cos\dfrac{\chi}{2} + \sin\dfrac{\chi}{2} b_0\right) \otimes \hat{q} \end{cases} \quad (24)$$

The pitch angle information complements well the direction measurement. However, the information does not permit to define a unique solution directly. In detail, the two equations defining the limit set of the observer

$$\sigma(q, q_f) = 0, \quad T(q_f) = T(q) \quad (25)$$

possess (exactly) four isolated solutions q_f parameterized under the form

$$\{(\cos \ell)\, q + (\sin \ell)\, (\boldsymbol{p}(b_0) \otimes q)\,,\ \ell \in [0, 2\pi]\}$$

with two possible solutions, $\ell = 0$ (corresponding to q) and $\ell = \ell_{\#}$ with $\ell_{\#} = \frac{\pi}{2} + e$

$$e = \arctan\left(\frac{bT_3(q) - 2aT_2(q)}{2(a^2+b^2)T(q) + acT_3(q) + 2bcT_2(q)}\right)$$

with $T_2(q) = q_1q_4 + q_2q_3$, $T_3(q) = 1 - 2(q_3^2 + q_4^2)$ which corresponds to $q^{\#}$. Provided some mild mathematical assumption on the nature of the flight, this observer converges as follows [22]: there exist $K, \lambda > 0$ s.t. $\forall t \geq 0$, $\min\left(|\delta(q,\overline{q})|, |\delta(-q,\overline{q})|, |\delta(q_{\#},\overline{q})|, |\delta(-q_{\#},\overline{q})|\right) < \varepsilon + K\exp^{-\lambda t}$. Therefore, the observer converges in the vicinity of two possible rotations, one corresponding to the truth (q or $-q$) and one to a shadow (undesirable) solution ($q_{\#}$ or $-q_{\#}$). This issue is not created by the observer design but is intrinsic to the measurements and Eq. (25) for which the two solutions are indistinguishable. Fortunately, the latter is easy to discriminate, as it yields values of yaw angles that are inconsistent with *a priori* knowledge of ballistics (e.g., corresponding to the projectile drifting to the opposite side of the expected Magnus effect induced by the rifled barrel or flying backward). In detail, this inconsistency depends on the orientation of b_0 w.r.t. the shooting «*plane*». Compared to q, $q_{\#}$ corresponds to a mirror attitude w.r.t. b_0 having the same pitch angle. A difficult to distinguish situation occurs when the angle between b_0 and the shooting direction is small (this situation occurs when the shot points strictly towards the magnetic North) because the difference between the actual yaw angle and its symmetric associated with $q_{\#}$ is small in such circumstances. Numerically, it is easy to favor the proper solution and forbid the shadow solution. It suffices to use the complementary filter (first two lines of the proposed observer) alone until σ is satisfyingly small, and then choose $\chi(0)$ so that $\overline{q}(0)$ obtained from $\hat{q}(0)$ gives the right solution.

6.5. Experimental results

The results are reported in Figs. 13a to 13c. Some level of noise and outliers can be seen propagating in the estimates. The overall performance is satisfactory. The innovation of the attitude observer converges to zero, the attitude estimation yielding a magnetic field measurement matching the real magnetometer output. These results were obtained using the radial accelerometer and the 3-axis magnetometer signals only, through the whole procedure presented above.

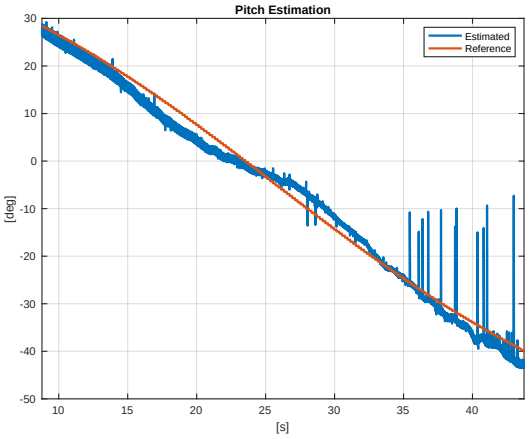

(a) Pitch angle.

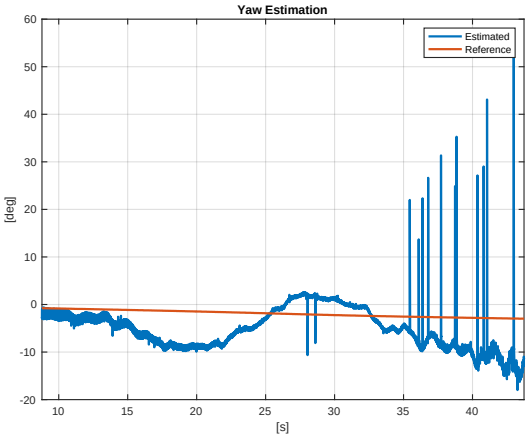

(b) Yaw angle.

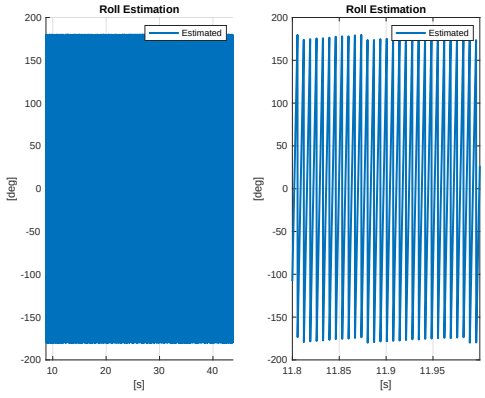

(c) Roll angle.

Figure 13: Attitude angle estimates [experimental results].

7. Conclusion

The article has offered an efficient method to estimate the attitude of an artillery shell in free-flight, using only 3-axis magnetometer and 3-axis accelerometer (only one axis was used). This method opens new trajectory estimation and control perspectives for such high-velocity symmetric projectiles using only embedded sensors. First, the velocity estimation obtained without any ground-based position radar offers novel ways to calibrate shells' aerodynamic models from on-board data instead of wind tunnels. Second, the in-flight velocity estimation is a valuable intermediate variable to estimate the projectile's position in a GNSS-denied environment. Even if the accuracy of the position will not be as good as with a GNSS receiver, it could be sufficient to make the projectile navigate to the basket where the seeker-head will detect the target.

The method presented in this article is novel because it uses the accelerometers in a new way, through frequency detection and a flight model. Experimental results have been presented, and comparisons with high-fidelity measurements from a ground-based position radar were provided. These results stress the feasibility of the method, which uses a minimal set of sensors and induces a computational burden that is compatible with the specifications of standard embedded processors.

Appendix A. Appendix: complex argument method for single-axis rotation rate estimation

The following method follows from [43, Theorem 3.1.]. Consider measurements of the form

$$y[k] = f(\psi[k]) + n[k] \in \mathbb{C}, \quad 1 \leq k \leq N$$

where f is a 2π-periodic function valued in $\mathbb{C}$ parameterizing a Jordan curve C, $\psi[k] = \psi(k\Delta t)$, $n[k]$ is a measurement noise. Assume that the interior region I to the boundary C is strictly convex. Assume that the noise n is uniformly bounded by ρ and that $|\psi[k+1] - \psi[k]|$ is uniformly bounded by $\Delta < \pi$. Then, the following sequence

$$\hat{\psi}_{z_0}[k] = \sum_{j=1}^{k-1} \arg_{-\pi} \frac{y[j+1] - z_0}{y[j] - z_0} \tag{A.1}$$

where z_0 is either i) the Chebyshev center of measurements, or ii) the polygon centroid, provides an estimate of $\psi[k]$, with an error than has an analytic upper bound.

This result can be readily applied to $Z_{mag} = Y_{mag2} + iY_{mag3}$, the curve C lying, approximately, on a circle. The derivative of the reconstructed phase provides an estimation of the spin rate.

References

[1] G. Wahba, Problem 65-1: a least squares estimate of spacecraft attitude, SIAM Review 7 (3) (1965) 409.

[2] M. D. Shuster, Kalman filtering of spacecraft attitude and the QUEST model, The Journal of the Astronautical Sciences 38 (3) (1990) 377–393.

[3] I. Y. Bar-Itzhack, REQUEST - a new recursive algorithm for attitude determination, Proceedings of the National Technical Meeting of The Institude of Navigation (1996) 699–706.

[4] J. L. Crassidis, F. L. Markley, Y. Cheng, Survey of nonlinear attitude estimation methods, Journal of Guidance, Control, and Dynamics 30 (1) (2007) 12–28.

[5] D. H. Titterton, J. L. Weston, Strapdown Inertial Navigation Technology, 2nd Edition, The American Institute of Aeronautics and Aeronautics, Reston, USA, 2004.

[6] R. Mahony, T. Hamel, J.-M. Pflimlin, Complementary filter design on the special orthogonal group SO(3), in: 44th IEEE Conference on Decision and Control, and the European Control Conference 2005, 2005, pp. 1477–1484.

[7] R. Mahony, T. Hamel, J.-M. Pflimlin, Nonlinear complementary filters on the special orthogonal group, IEEE Transactions on Automatic Control 53 (5) (2008) 1203–1218.

[8] R. Mahony, T. Hamel, P. Morin, E. Malis, Nonlinear complementary filters on the special linear group, International Journal of Control 85 (10) (2012) 1557–1573.

[9] M.-D. Hua, Attitude estimation for accelerated vehicles using gps/ins measurements, Control Engineering Practice 18 (7) (2010) 723–732.

[10] F. Königseder, W. Kemmetmüller, A. Kugi, Attitude estimation using redundant inertial measurement units for the control of a camera stabilization platform, IEEE Transactions on Control Systems Technology 24 (5) (2016) 1837–1844.

[11] L. Benziane, A. El Hadri, A. Seba, A. Benallegue, Y. Chitour, Attitude estimation and control using linearlike complementary filters: theory and experiment, IEEE Transactions on Control Systems Technology 24 (6) (2016) 2133–2140.

[12] A. Tayebi, A. Roberts, A. Benallegue, Inertial vector measurements based velocity-free attitude stabilization, IEEE Transactions on Automatic Control 58 (11) (2013) 2893–2898.

[13] R. Kottath, P. Narkhede, V. Kumar, V. Karar, S. Poddar, Multiple model adaptive complementary filter for attitude estimation, Aerospace Science and Technology 69 (2017) 574–581.

[14] C. G. Mayhew, R. G. Sanfelice, A. R. Teel, Quaternion-based hybrid control for robust global attitude tracking, IEEE Transactions on Automatic control 56 (11) (2011) 2555–2566.

[15] J. Reis, P. Batista, P. Oliveira, C. Silvestre, Attitude estimation using high-grade gyroscopes, Control Engineering Practice 92 (2019) 104134.
[16] P. Martin, I. Sarras, A global observer for attitude and gyro biases from vector measurements, IFAC-PapersOnLine 50 (1) (2017) 15409–15415.
[17] K. Gaber, M. B. E. Mashade, G. A. A. Aziz, Real-time implementation of a robust simplified intelligent proportional–integral control for cubesat attitude determination system, Control Engineering Practice 98 (2020) 104377.
[18] S. Bertrand, T. Hamel, H. Piet-Lahanier, R. Mahony, Attitude tracking of rigid bodies on the special orthogonal group with bounded partial state feedback, in: Proceedings of the 48h Conference on Decision and Control, IEEE, 2009, pp. 2972–2977.
[19] S. Changey, E. Pecheur, P. Wey, Real time estimation of supersonic projectile roll angle using magnetometers: In-lab experimental validation, IFAC Proceedings Volumes 42 (5) (2009) 123–127.
[20] R. L. McCoy, Modern exterior ballistics, 2nd Edition, Schiffer, 1998.
[21] R. H. Fowler, E. G. Gallop, C. N. H. Lock, H. W. Richmond, The aerodynamics of a spinning shell, Proceedings of the Royal Society of London. Series A, Containing Papers of a Mathematical and Physical Character 98 (690) (1920) 199–205.
[22] A. Fiot, Attitude estimation of an artillery shell in free-flight from accelerometers and magnetometers, Ph.D. thesis, MINES ParisTech, PSL University, France (2020).
[23] J. L. Kelley, E. J. McShane, On the motion of a projectile with small or slowly changing yaw, Ballistics Research Laboratories Rep. No. 446, Dec. 1944 (1944).
[24] R. H. Kent, Notes on a theory of spinning shell, Tech. rep., Ballistics Research Laboratories Rep. No. 898. 1954 (1954).
[25] C. H. Murphy, Free flight motion of symmetric missiles, Tech. rep., Army Ballistic Research Lab Aberdeen Proving Ground MD (1963).
[26] V. Fleck, Introduction à la balistique extérieure avec exercices, Cours de balistique extérieure, Coëtquidan (2005).
[27] A. Fiot, S. Changey, C. Combettes, N. Petit, A gyroless adaptation of attitude complementary filtering, in: Proc. of the European Control Conference (ECC), 2019, pp. 2121–2127.
[28] M. Costello, T. Jitpraphai, Determining angular velocity and angular acceleration of projectiles using triaxial acceleration measurements, Journal of spacecraft and rockets 39 (1) (2002) 73–80.
[29] L. Magnis, N. Petit, Angular velocity nonlinear observer from single vector measurements, Automatic Control, IEEE Transactions on 61 (9) (2016) 2473–2483.
[30] J. Shang, Z. Deng, M. Fu, S. Wang, A high-spin rate measurement method for projectiles using a magnetoresistive sensor based on time-frequency domain analysis, Sensors 16 (6) (2016) 894.
[31] L. Magnis, N. Petit, Angular velocity nonlinear observer from vector measurements, Automatica 75 (2017) 46–53.
[32] P. Cardou, J. Angeles, Estimating the angular velocity of a rigid body moving in the plane from tangential and centripetal acceleration measurements, Multibody System Dynamics 19 (4) (2008) 383–406.
[33] S. Mallat, A wavelet tour of signal processing: the sparse way, Academic Press, 2008.
[34] V. F. Pisarenko, The retrieval of harmonics from a covariance function, Geophysical Journal International 33 (3) (1973) 347–366.
[35] R. Schmidt, Multiple emitter location and signal parameter estimation, IEEE Transactions on Antennas and Propagation 34 (3) (1986) 276–280. doi:10.1109/TAP.1986.1143830.
[36] M. H. Hayes, Statistical digital signal processing and modeling, John Wiley & Sons, New York, 1996.
[37] P. Stoica, T. Soderstrom, Statistical analysis of MUSIC and subspace rotation estimates of sinusoidal frequencies, IEEE Transactions on Signal Processing 39 (8) (1991) 1836–1847. doi:10.1109/78.91154.
[38] J. Gerbaux, N. Petit, Analysis of the MUSIC estimator for the detection of frequencies in sinusoidal signals, Tech. rep., MINES Paris, PSL University (2021).
[39] N. N. Krasovskii, Problems of the theory of Stability of Motion, MIR, translated by Stanford University Press, 1963.
[40] D. Carnevale, D. Karagiannis, A. Astolfi, Reduced-order observer design for systems with non-monotonic nonlinearities, in: Proceedings of the 45th Conference on Decision and Control, IEEE, 2006, pp. 5269–5274.
[41] A. Alessandri, P. Coletta, Switching observers for continuous-time and discrete-time linear systems, in: Proceedings of the American Control Conference, IEEE, 2001, pp. 2516–2521.
[42] A. A. Chunodkar, M. R. Akella, Switching angular velocity observer for rigid-body attitude stabilization and tracking control, Journal of Guidance, Control, and Dynamics 37 (3) (2014) 869–878.
[43] L. Magnis, Estimation of angular rate from direction sensors, Ph.D. thesis, MINES ParisTech (2016).